Strong Magnetocrystalline Anisotropy Arising from Metal–Ligand Covalency in a Metal–Organic Candidate for 2D Magnetic Order

Yiran Wang,[†,§] Michael E. Ziebel,[‡,§] Lei Sun,[†] J. Tyler Gish,[¶] Tyler J. Pearson,[†] Xue-Zeng Lu,[¶] Agnes E. Thorarinsdottir,[†] Mark C. Hersam,[†,¶] Jeffrey R. Long,[‡,∥,⊥,*] Danna E. Freedman,[†,#,*] James M. Rondinelli,[¶,*] Danilo Puggioni,[¶,*] and T. David Harris[†,‡,*]

[†]Department of Chemistry and [¶]Department of Materials Science and Engineering, Northwestern University, Evanston, Illinois 60208, United States

[‡]Department of Chemistry and [∥]Department of Chemical and Biomolecular Engineering, University of California, Berkeley, California 94720, United States

[⊥]Materials Sciences Division, Lawrence Berkeley National Laboratory, Berkeley, California, 94720, United States

[#]Department of Chemistry, Massachusetts Institute of Technology, Cambridge, Massachusetts 02139, United States

ABSTRACT: Layered metal–organic frameworks are promising candidates for new two-dimensional magnets, as their synthetic programmability of these materials can provide a route to diverse structural and electronic properties. However, such framework materials typically lack the heavy elements that engender magnetocrystalline anisotropy in the monolayer ferromagnets reported to date. Alternative sources of magnetic anisotropy are therefore needed in these materials. Here, we report the synthesis of single crystals of the framework material $(NMe_4)_2[Fe_2L_3]$ (H_2L = 3,6-dichloro-2,5-dihydroxybenzoquinone) and evaluate the angular dependence of its magnetic properties. Oriented-crystal magnetization measurements reveal strong uniaxial anisotropy, where the easy axis is aligned with the crystallographic *c* axis. While the spin carriers of this structure are isotropic $S = {}^5/_2$ Fe^{III} metal centers and $S = ½$ organic linkers, the anisotropy energy of the framework material is comparable to that of reported 2D ferromagnets. Density functional theory calculations indicate that the observed magnetocrystalline anisotropy arises from ligand-to-metal charge transfer that enhances the magnetic anisotropy of the otherwise isotropic Fe centers, suggesting that metal–ligand covalency can be utilized as a general additive for the development of 2D magnets. These results show the possibility for $(NMe_4)_2[Fe_2L_3]$ to retain magnetic order down to the 2D monolayer limit. In addition, the combination of large magnetic anisotropy and semiconducting character in $(NMe_4)_2[Fe_2L_3]$ highlights its potential as a new 2D magnetic semiconductor.

INTRODUCTION

Since the discovery of graphene, two-dimensional (2D) materials that can be exfoliated down to the monolayer limit have received ever-increasing attention.[1–3] Such materials can exhibit diverse phenomena that differ from those observed in their bulk counterparts, and they could find use in numerous electronic, optical, and electrochemical applications.[4–6] Further, the properties of 2D materials can be controlled through their incorporation into van der Waals heterostructures or through electrical gating, thereby providing a vast phase space for the exploration of materials properties.[7–9] Within the class of 2D materials, magnetic properties have been studied much less than the aforementioned properties, despite the potential for integrating these materials within novel magneto-optical or magneto-electronic devices.[10] Indeed, ferromagnetic order at the monolayer limit was only recently experimentally demonstrated.[11–13] Although the number of authentic 2D ferromagnets remains exceedingly small, this discovery has already launched new research directions to control and utilize the magnetic properties of these materials.[14–17]

The development of new layered magnetic materials is of great technological value, with magnetic semiconductors being of particular interest. In the bulk phase, the spin-polarized transport and magneto-optical properties of magnetic semiconductors are critical in devices such as magnetic tunnel junctions and spin field-effect transistors,[18–20] and the ability to tune the magnetic ordering temperature and coercivity of these materials with electric fields provides advantages over metallic and insulating magnetic materials.[21,22] In particular, extending the properties of magnetic semiconductors into van der Waals heterostructure devices could give rise to new applications in spin- and valleytronics.[23–25]

Metal–organic frameworks represent a promising materials platform to develop 2D magnetic semiconductors.[26] In comparison to conventional inorganic solids, metal–organic frameworks offer greatly enhanced chemical versatility, as their electronic, magnetic, and optical properties can be predictively and widely modulated through metal ion or organic linker substitution.[27–29] This synthetic programmability enables the elucidation of structure–property relationships to guide the design of new materials. Recently, a number of layered metal–organic materials have been predicted or demonstrated to display magnetic order and semiconducting character in the bulk, though none have been studied at the 2D limit.[30–37] The Mermin-Wagner theorem suggests that long-range magnetic order in low-dimensional (1D or 2D) systems is strongly suppressed by thermal fluctuations at finite temperatures in the absence of magnetic anisotropy.[38] Specifically, for a material to retain its magnetic order when exfoliated to the 2D limit, it must

possess intrinsic magnetocrystalline anisotropy, where the crystal structure of the material dictates the symmetry of the anisotropy.[39] For example, in CrI_3, strong uniaxial anisotropy (0.25 meV/Cr) enables monolayer ferromagnetic ordering with a T_C of 45 K,[11,40,41] and higher magnetic ordering temperatures have been achieved in 2D materials with increased anisotropy energies.[42] Magnetocrystalline anisotropy arises from spin–orbit coupling, typically in the form of single-ion anisotropy, as in rare-earth magnets containing magnetic ions with large spin–orbit coupling,[43] or as exchange anisotropy, as in CrI_3 where super exchange interactions mediated by iodide ions with large spin–orbit coupling generate anisotropy.[40] Because spin–orbit coupling is the primary contributor to magnetocrystalline anisotropy, and because metal–organic magnets lack the heavy elements that provide strong spin–orbit coupling and engender anisotropy in most reported 2D magnets,[40,44] detailed characterization of the magnetic anisotropy of metal–organic magnets is needed to assess their potential as new candidates for 2D magnetic semiconductors.

To this end, one particularly promising class of materials for further study is the family of layered, honeycomb framework materials based on the ligand 2,5-dihydroxybenzoquinone and its derivatives.[45] These materials can be synthesized with a large number of different metal centers or organic linkers, giving rise to a diverse range of electronic and magnetic phenomena,[46–52] and post-synthetic reduction or oxidation of these materials enables further modification of their properties.[32,53,54] Of particular interest is the framework material $(H_2NMe_2)_2[Fe_2L_3]\cdot 6DMF\cdot 2H_2O$ (**1**) (H_2L = 3,6-dichloro-2,5-dihydroxybenzoquinone), which is a ferrimagnetic semiconductor with a characteristic temperature of T_C = 80 K.[48] The conductivity of this material arises from organic linker-centered mixed valency, while the magnetic order arises from strong metal–radical coupling. Both the magnetic ordering temperature and conductivity of this material can be readily modified through post-synthetic reduction. Further, the large number of electrochemically accessible redox states suggests that the magnetic and electronic properties of monolayers of **1** could be easily be tuned in an electrically gated device.[32,55] Importantly, while the spin carriers of **1** are isotropic $S = {}^5/_2$ Fe^{III} metal centers and $S = {}^1/_2$ $L^{3-\bullet}$ linkers, magnetic measurements on non-oriented powders reveal a large coercive field of H_c = 2630 Oe at 1.8 K, suggesting the presence of magnetic anisotropy.[48]

Although single crystals of **1** are too small to perform oriented magnetic measurements, the chemical versatility of these materials enables the exploration of related compounds for which large single crystals can be grown. Herein, we report the synthesis and magnetic characterization of the material $(NMe_4)_2[Fe_2L_3]\cdot 7DMF$ (**2**), which contains a 2D honeycomb framework isostructural to that in **1** with a similar electronic and magnetic structure. Oriented-crystal magnetic measurements reveal strong uniaxial magnetocrystalline anisotropy, with the easy axis of magnetization aligned perpendicular to the 2D layers. The calculated anisotropy energy is comparable to that of CrI_3, and density functional theory (DFT) calculations suggest that the anisotropy originates from the covalency of the Fe^{III}–$L^{3-\bullet}$ interaction. Together, these results illustrate the potential of **2** to exhibit magnetic order at the monolayer limit.

RESULTS AND DISCUSSION

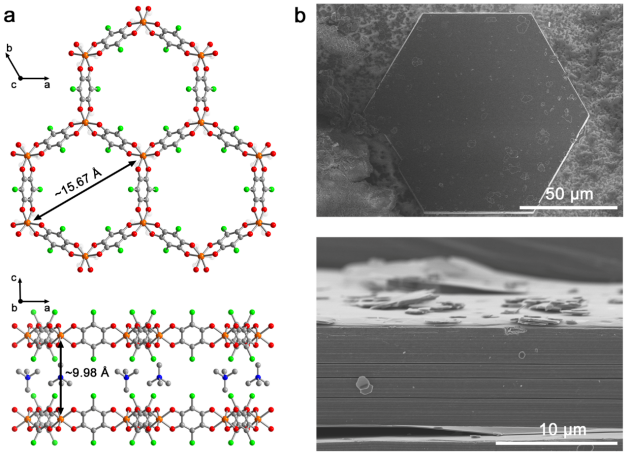

Figure 1. (a) Crystal structure of **2**, as viewed along the crystallographic *c* axis (upper) and *b* axis (lower), with selected Fe···Fe distances highlighted. Orange, green, red, blue, and gray spheres represent Fe, Cl, O, N, and C atoms, respectively; H atoms and DMF molecules are omitted for clarity. **(b)** SEM images of **2**, as viewed along the crystallographic *c* axis (upper) and *b* axis (lower).

Synthesis, Structure, and Bulk Magnetic Properties. Black hexagonal plate-shaped crystals of **2** were grown by heating a mixture of $Fe(BF_4)_2\cdot 6H_2O$, H_2L, and $(NMe_4)BF_4$ in DMF at 130 °C for two days. While similar syntheses for **1** yielded crystals with typical widths of ca. 30 µm,[48] this synthetic procedure generated crystals of **2** with widths as large as 100–200 µm and thicknesses as large as 5–20 µm. Single-crystal X-ray diffraction analysis revealed that **2** crystallizes in the trigonal space group $P\bar{3}1m$, with a structure comprising extended anionic layers of $[Fe_2L_3]^{2-}$ separated by NMe_4^+ cations, with an interlayer d_{Fe-Fe} of 9.9759(18) Å (Figure 1a). The position of the cation between the anionic layers, rather than within the pore of the framework, results in a 14% increase in the interlayer spacing compared to **1**, which should further reduce the strength of interlayer magnetic coupling and thus enhance the 2D characteristics of **2**. The DMF solvent molecules are disordered in the lattice, and their presence was confirmed by elemental and thermogravimetric analyses (Figure S1). The anionic metal–organic layer features a honeycomb network within the crystallographic *ab* plane, and the layers stack in a fully eclipsed manner to generate hexagonal 1D channels along the crystallographic *c* axis with pore diameters of 15.6717(21) Å. The former manifests in hexagonal crystal faces and the latter coincides with the shorter dimension of the crystal, as verified by face indexing of the crystals (Figure S2). Scanning electron microscopy (SEM) studies confirmed the layered structure of **2** (Figure 1b). Within the crystallographic *ab* plane, the crystal exhibits a uniform hexagonal morphology; in contrast, the layers are loosely packed with visible striations running perpendicular to the *c* axis, indicating the potential for exfoliation of the material. Taken together, these structural observations highlight the 2D nature of **2**, suggesting it as a suitable system to investigate magnetocrystalline anisotropy.

Mössbauer and Raman spectroscopy were used to confirm that the metal–organic layers of **2** possess a similar electronic structure to those in **1**. Mössbauer spectroscopy confirms the presence of a high-spin Fe^{III} center with a similar isomer shift (δ = 0.574(1) mm/s) and quadrupole splitting (ΔE_Q = 1.125(5) mm/s) as in **1** (Figure S4), and Raman spectroscopy indicates partial ligand reduction and electron delocalization (Figure

S5).[48] Together, these results suggest an *in situ* metal-to-ligand electron transfer during framework formation and a formal approximate composition of $[Fe^{III}_2(L^{2-})(L^{3-\bullet})_2]^{2-}$. This formulation is further supported by the observation of an intervalence charge-transfer band in the near-infrared diffuse reflectance spectrum and a room-temperature electronic conductivity comparable to that of **1** (Figures S6 and S7). As in **1**, the presence of linkers with substantial radical character in **2** results in strong direct exchange between Fe^{III} centers and ligand-based spins, leading to long-range ferrimagnetic order below 34 K (Figure 2). A small frequency dependence in the *ac* susceptibility indicates the presence of some glassy dynamics in **2**, but the observation of magnetic saturation at high fields suggests that **2** is best described as a glassy ferrimagnet rather than a disordered spin glass (S8–S13; see Supporting Information for an extended discussion of the magnetic properties of non-oriented samples of **2**). While the ordering temperature of **2** is lower than that of **1**, potentially due to the larger interlayer spacing or slight differences in the degree of linker reduction (See extended discussion in the Supporting Information), their coercive fields at 1.8 K are nevertheless similar (2630 and 3013 Oe for **1** and **2**, respectively) (Figure 2, inset). Magnetic coercivity cannot be directly correlated to magnetic anisotropy, but the coercive fields observed here suggest the presence of substantial anisotropy in **1** and **2**, despite containing only isotropic $S = {}^5/_2$ Fe^{III}- and $S = {}^1/_2$ linker-based spin carriers.[56] In contrast, a three-dimensional (3D) structural isomer exhibits a coercive field of only 100 Oe at 2 K,[57] while the isostructural framework material $Na_3(NMe_4)_2[Mn_2L_3]$, which possesses similar $S = {}^5/_2$ metal centers and $S = {}^1/_2$ linkers, displays a coercive field of only 300 Oe at 1.8 K.[54] Together, these results suggest that neither the metal–ligand covalency nor the layered structure of **1** and **2** can alone explain the coercivities of the materials, although the combination of these factors may give rise to magnetocrystalline anisotropy.

Oriented-Crystal Magnetic Measurements. To probe the magnetocrystalline anisotropy of **2**, magnetic data were collected for single crystals oriented along selected crystallographic directions. Here, a collection of single crystals

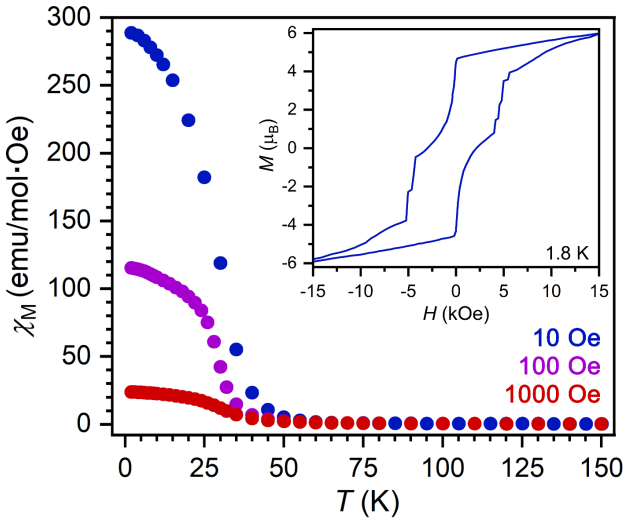

Figure 2. Variable-temperature field-cooled dc magnetic susceptibility data for a randomly oriented sample of **2** collected under applied magnetic fields of 10 (blue), 100 (purple), and 1000 (red) Oe. Inset: Magnetic hysteresis measurements for a randomly oriented sample of **2**, collected at 1.8 K with a field sweep rate of 1.94 Oe/s.

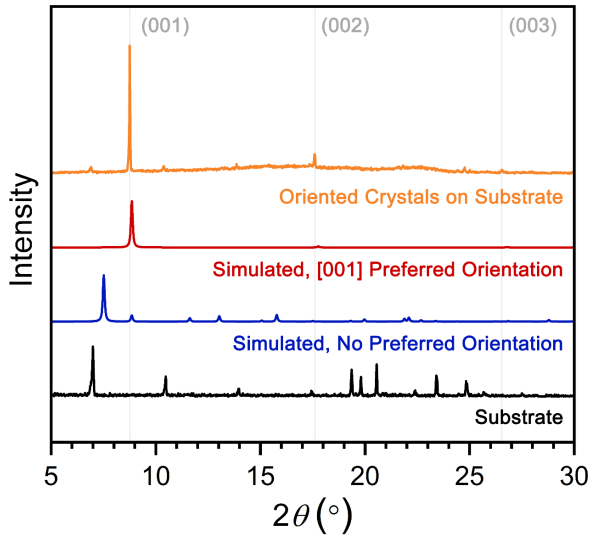

Figure 3. Powder X-ray diffraction data for the oriented crystals of **2** (orange), simulated data for **2** with (red) or without (blue) [001] preferred orientation, and data for the sample substrate. Gray lines represent the (001), (002), and (003) reflections of **2**. Slight differences between experimental and simulated peak positions are due to the different collection temperatures for powder (298 K) and single crystal (250 K) X-ray diffraction data. All data were collected or simulated with a wavelength of 1.54056 Å.

was drop cast onto a 3 mm × 5 mm sapphire wafer and then restrained in eicosane (Figure S14). Powder X-ray diffraction data, collected at a wavelength of 1.5406 Å, for the wafer sample showed strong preferred orientation along the [001] crystallographic direction, confirming that the vast majority of the crystals were aligned with the *c* axis perpendicular to the substrate (Figure 3). The sample wafer was mounted on a horizontal rotator sample rod that allows adjustments of the relative angle between the crystallographic *c* axis of **2** and the applied magnetic field, and the projection of magnetization (M_z) to the direction of the applied field was measured as a function of angle, temperature, and field strength.

Variable-field dc magnetization data collected at 1.8 K reveal distinct magnetic behavior for different substrate orientations (Figure 4a). When the field is applied parallel to the *c* axis, perpendicular to the 2D layers ($H \parallel c$), M_z gradually increases with field up to 0.8 T, at which point a rapid increase is observed, reaching the saturation magnetization near 1.2 T. The rapid increase in magnetization occurs at H_c (see discussion of hysteresis below), suggesting that the small magnetization observed at lower fields corresponds to an even distribution of crystals with magnetizations aligned parallel and antiparallel to the applied field. Here, applied magnetic field strengths below H_c are too weak to overcome the magnetic anisotropy energy. When the field strength reaches H_c, the antiparallel magnetizations flip, and the overall magnetization becomes saturated. In contrast, when the magnetic field is applied perpendicular to the *c* axis, parallel to the 2D layers ($H \perp c$), M_z gradually increases with field up to ~5 T, at which point saturation behavior is observed. A small kink in the magnetization at 0.8 T most likely corresponds to a small number of crystals with their *c* axis parallel to the substrate. These results indicate a clear magnetocrystalline anisotropy in **2**, with an easy axis of magnetization aligned with the *c* axis and a hard plane aligned with the *ab* plane.

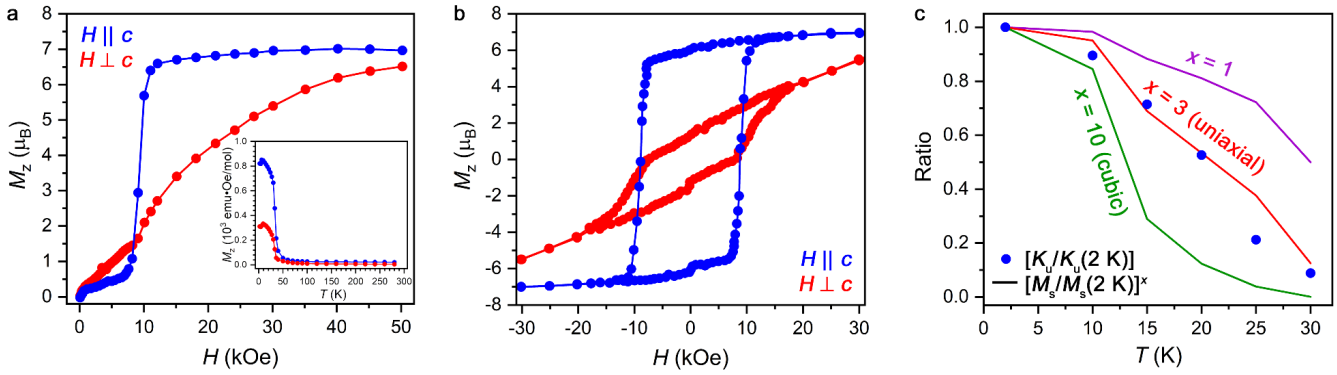

Figure 4. (a) Variable-field dc magnetization data for the oriented single-crystal sample of **2**, collected at 1.8 K. Inset: Variable-temperature dc magnetization data for the oriented single-crystal sample. Blue and red data correspond to data with $H \parallel c$ or $H \perp c$, respectively. Collected at a field of 10 Oe. **(b)** Variable-field magnetic hysteresis data for the oriented-crystal sample of **2**, collected at 1.8 K. Blue and red lines are guides to the eye. Intermediate angle data are shown is Figures S15–S17, and the full hysteresis loops are shown in Figure S19. **(c)** The ratio $K_u(T)/K_u(2\text{ K})$ (blue dots) as a function of temperature, compared to the ratio $[M_s/M_s(2\text{ K})]^x$ for x = 1, 3, or 10 (maroon, red, and pink lines). The temperature dependence of the anisotropy constant most closely scales to the third power of $M_s/M_s(2\text{ K})$, characteristic of uniaxial anisotropy.

The presence of an easy axis is further demonstrated by magnetic hysteresis data collected at 1.8 K (Figure 4b). For $H \parallel c$, the hysteresis loop displays a rectangular shape, with H_c = 8845 Oe at a sweep rate of 1.98 Oe/s. This shape profile indicates that the magnetic domains remain aligned along the easy axis and reverse abruptly at the coercive field (Figures 4b and S17). In contrast, for $H \perp c$, the hysteresis loop displays a spindle shape, with H_c = 8042 Oe with a sweep rate of 1.88 Oe/s. Unlike the rapid switching of the magnetization observed with $H \parallel c$, the gradual increase and decrease in the magnetization for $H \perp c$ indicate a gradual reversal of the magnetic domains with changing field.[58] The differences between the two hysteresis loops can be quantified using the squareness ratio, which is the ratio of the remnant magnetization (M_r) to the saturation magnetization (M_s). The squareness ratios M_r/M_s for $H \parallel c$ and $H \perp c$ are 0.86 and 0.20, respectively, which indicate that the magnetization at zero field is better preserved when the magnetic field is parallel to the c axis. Films of the commercial permanent magnet $SmCo_5$ with large magnetic anisotropy display similar differences in squareness ratio for hysteresis loops measured along the easy axis (0.96) and hard plane (0.15).[59] As such, the observed differences for **2** further support the presence of an easy axis of magnetization aligned along the c axis.

Notably, the hysteresis loops for the aligned crystals differ substantially from those observed for randomly oriented powders. The coercivity is greatly enhanced for the aligned samples, and the sharp drop in the magnetization observed at zero field for the randomly oriented samples is no longer observed for the aligned crystals. In molecules, sharp drops in the magnetization at zero field are typically associated with quantum tunneling, which would not be expected in a strongly coupled bulk material such as **2**. Additional studies are required to better understand the zero-field drop in randomly oriented samples. Nevertheless, the enhanced coercivities of the aligned samples at 1.8 K are among the highest yet observed for metal–organic framework magnets.[37,60–65]

To quantify the magnetocrystalline anisotropy energy (E_a) of **2**, we determined the uniaxial anisotropy constant K_u using the Stoner-Wohlfarth model:

$$\frac{2K_u}{M_s} = \mu_0 H_{sat} \qquad (1)$$

which assumes a fully magnetized, single-domain state, where M_s is the saturation magnetization, and H_{sat} is the magnetic field above which the sample is fully magnetized.[58] The values of M_s and H_{sat} were obtained by fitting the magnetization data with $H \perp c$ (see details in Supporting Information). This model yields a value of K_u = 50 kJ/m^3 at 1.8 K. Similar anisotropy constants were obtained by fitting the data using the Sucksmith-Thompson method (see Supporting Information).[66,67]

To further assess the uniaxial character of the magnetic anisotropy in **2**, we performed variable-temperature magnetization measurements to determine the temperature dependence of K_u (Figure 4c). In the classical model developed by Zener,[68] the relationship between the anisotropy energy and the saturation magnetization can be described as:

$$\langle K_n \rangle \propto M_s^{\frac{n(n+1)}{2}} \qquad (2)$$

where $\langle K_n \rangle$ represents the anisotropy expectation value for the n^{th} power angular function, which is determined by the crystal symmetry. For uniaxial and cubic symmetry, the value of n is 2 and 4, respectively, corresponding to exponents of 3 and 10 in equation 2. As expected for a uniaxial magnet, the value of $[K_u/K_u(2\text{ K})]$ for **2** scales with $[M_s/M_s(2\text{ K})]^3$.[68,69] These results demonstrate the strong magnetocrystalline anisotropy of **2** with the easy axis aligned with the crystallographic c axis.

Because of the low-density framework structure of **2**, direct comparison of its volumetric anisotropy constants to those of other materials does not accurately reflect the relative anisotropies per formula unit. Converting the uniaxial anisotropy constant to a per-atom basis yields a value of 0.25 meV/Fe atom, which is similar to or larger than the analogous values obtained for materials that have been isolated as monolayer ferromagnets, including CrI_3 (0.25 meV/Cr) and $Cr_2Ge_2Te_6$ (0.03 meV/Cr).[41,70] Given that the calculated anisotropy constants for **2** were obtained for a collection of oriented crystals, rather than for one crystal, the value reported here likely represents a lower limit of the true anisotropy energy. The observation of substantial anisotropy in **2** is remarkable given that its magnetic ions consist of $S = {}^5/_2$ Fe^{III} ions and organic radical linkers, which are both expected to be highly isotropic. Indeed, magnetocrystalline anisotropy in most Fe^{III} materials is dominated by weak single-ion anisotropy generated by Fe^{III} excited states. Cubic Fe^{III} oxides, such as $BiFeO_3$ and

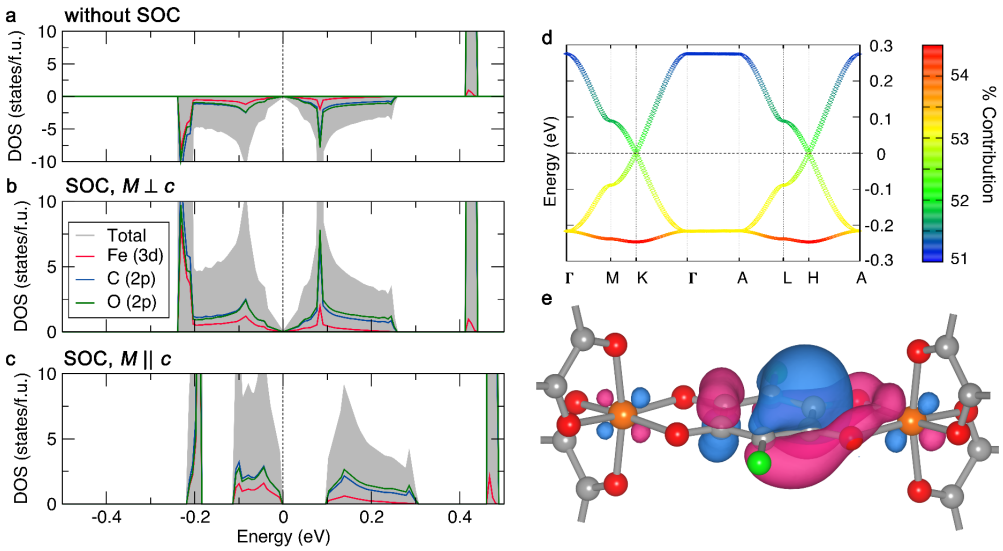

Figure 5. (**a**–**c**) Density of states (DOS) of **2** without spin–orbit coupling (SOC) (a) or with spin–orbit coupling and the local magnetic moment aligned along the crystallographic *a*-axis (b) or *c*-axis (c). The Fermi level (a and b) or valence band maximum (c) is set to 0 eV. (**d**–**e**) The Wannier interpolation of the spin-down channel band structure of **2** without SOC. The color field represents the contribution of the maximally localized Wannier function (MLWF) (e) to the Bloch states in the three spin-down bands near the Fermi level. Blue and purple lobes correspond to positive and negative values of the MLWF. The dashed line indicates the Fermi level.

$Y_3Fe_5O_{12}$,[71,72] have calculated or experimental anisotropy energies of less than 25 μeV/Fe. Similarly, anisotropy energies in layered $FeCl_3$-graphite intercalation compounds have been estimated to be 10-20 μeV/Fe.[73] Some hexagonal ferrites, such as $BaFe_{12}O_{19}$, do possess anisotropy energies of similar magnitude to **2**;[74] however, anisotropy in these materials is largely derived from the single-ion anisotropy of trigonal bipyramidal Fe^{III} sites, which are not present in **2**, and dipole-dipole interactions, which should be much weaker in **2** than in oxide materials due to the much larger distances between spin centers.[75,76] Furthermore, **2** lacks the heavy elements that can provide magnetic anisotropy via strong spin-orbit coupling. Consequently, while the strength of magnetocrystalline anisotropy elucidated for **2** is likely sufficient for magnetic ordering to persist down to the monolayer limit, we sought to better understand the origin of magnetic anisotropy in **2** to inform the future design of 2D metal–organic magnets.

Electronic Structure Calculations. Spin-polarized density functional theory (DFT) calculations were used to understand the electronic origin of magnetic anisotropy in **2** (see Supporting Information for details). The electronic structure of **2** was initially modeled at the DFT-GGA+*U* level, neglecting spin–orbit coupling (SOC), with U = 5 eV and ferromagnetic alignment of high-spin Fe^{III} spins. For simplicity, cations were removed from the structure and a uniform background charge was used to account for charge balance. DFT calculations were performed for a dianionic unit cell (as in **2**) and for a neutral unit cell. The density of states (DOS) calculated for **2** (Figure 5a) indicates semimetallic behavior with strong hybridization of the 2p states of C and O atoms with the 3d states of Fe atoms at the top and bottom of the valence and conduction band, respectively, indicative of metal–ligand covalency. Interestingly, the electronic band structure shows band crossings at the Fermi level (Figure 5d) yielding a Dirac-point Fermi surface, though, experimentally, **2** is a semiconductor, which may indicate that a band gap emerges due to spin–orbit coupling (see discussion below), or potentially due to structural disorder and polaron formation. Despite this discrepancy, the calculated band structure accurately depicts the orbitals that contribute to the valence and conduction band and the local electronic structure of the framework. As expected, while the neutral model exhibits a total magnetization of 10 μ_B per unit cell, the dianionic model shows a total magnetization of 8 μ_B, in agreement with experimental results. The comparison between the spin density of neutral and dianionic unit cells confirms that the latter contains high-spin Fe^{III} ions with spin-up character, while the organic linkers exhibit spin-down density in π* orbitals, in accord with the experimentally determined electronic structure (Figure S22).

Next, we included SOC in the calculations and considered magnetization aligned along the crystallographic *a* or *c* axis. For both cases, the DOS and electronic band structure are very similar to those calculated without the inclusion of SOC (Figures 5 and S24), exhibiting van Hove singularities in proximity to the Fermi level. When the magnetization is aligned parallel to the *c* axis, however, the band crossing is removed and a band gap of ~80 meV opens (Fig. S24c). We note that this band gap is smaller than the one estimated from optical measurements (~0.35 eV, Figure S6) and variable-temperature transport measurements on **1** (0.26 eV),[32] suggesting that other factors may also contribute to the semiconducting character of **2**. The gap introduced by SOC stabilizes the energy of this orientation of the magnetization by 1.56 meV/Fe atom relative to the configuration with the magnetization along the *a* axis, which remains semimetallic. This energy difference supports the possibility that the experimentally determined value, 0.25 meV/Fe, may indeed underestimate the anisotropy of **2**. Note that the absence of the NMe_4^+ cations in the calculated structure and possible structural disorder in the measured crystals may also contribute to the difference between experiment and theory.

For both magnetization directions, comparison of the charge density for the dianionic and neutral unit cells reveals no substantial differences upon incorporation of SOC (Figure S23). However, comparison of the charge density for the dianionic unit cells with *a*- and *c*-oriented magnetization reveal a small change in the charge distribution. Specifically, the *a*-oriented configuration contains increased charge density in the π-orbitals of the organic linkers, while the *c*-oriented electronic structure

contains increased charge density in σ-bonding orbitals, indicating ligand-to-metal charge transfer (Figure S23). Under the convention that the net spin on each Fe center is α-spin, this charge transfer introduces a small β-spin density onto the otherwise-isotropic Fe^{III} centers, thereby engendering significant magnetic anisotropy. Similar metal–ligand covalency has been invoked in 2D chromium–pyrazine frameworks, including one example that shows a remarkable coercivity of 7500 Oe at 27 °C.[34,37]

To test this hypothesis, we used maximally localized Wannier functions (MLWFs) to interrogate the real space wave functions of the participating states (see Supporting Information for details). For **2**, Wannierization of the calculated electronic band structures converts the extended Bloch orbitals to localized, real-space molecular-like orbitals that allow us to visualize the dominant bonding interactions in the valence and conduction bands.[77] Ideally, it would be possible to visualize the bonding interaction for the electronic structure magnetized along the *c* axis, but the complex nature of the spinor Wannier functions makes their visualization problematic.[78] However, the DOS and electronic band structure with and without SOC are very similar (Figures 5 and S24). Therefore, we proceeded by Wannierizing the electronic band structure calculated without SOC to use scalar Wannier functions that are easily representable. In particular, we focused on the spin-down channel that forms the low energy states. The calculated MLWF bands are nearly indistinguishable from the DFT bands (Figure S25), confirming the high quality of the Wannierization. While several MLWFs contribute to the three spin-down bands near the Fermi level, the main contribution (>50%, Figure 5d) originates from the MLWF depicted in Figure 5e. This MWLF is largely localized on the π-orbitals of the organic linkers, but shows clear evidence of π-donation into Fe 3d orbitals. This result further supports the hypothesis that metal–ligand covalency and ligand-to-metal charge transfer enhance the magnetocrystalline anisotropy of the Fe centers in **2**. A local molecular orbital model of this charge transfer phenomenon is depicted in Figure S26.

Similar charge transfer would not be expected in the isostructural Mn^{II} framework, likely explaining its low coercivity.[54] Additionally, while ligand-to-metal charge transfer may occur in the 3D cubic structural isomer of **2**, its isotropic crystal structure limits its magnetic anisotropy and thus results in a low coercivity.[57] As such, both the layered crystal structure and the covalent bonding of **2** are critical to achieve the large magnetic coercivity and magnetocrystalline anisotropy.

Mechanical Exfoliation of $(NMe_4)_2[Fe_2L_3]$. Based on this experimental evidence for magnetocrystalline anisotropy presented in **2**, the magnetic properties of mechanically exfoliated layers merit further characterization. Similar metal–chloranilate framework materials have been exfoliated in solution, but monolayers have not been isolated.[79,80] To assess if monolayers of **2** could be directly isolated using mechanical exfoliation, we attempted exfoliation using the Scotch tape method. Atomic force microscopy (AFM) images of the exfoliated material revealed micron-sized flakes with thicknesses as low as 35 nm, corresponding to ~35 layers, and step edges of 2 nm, corresponding to bilayers of **2** (Figure 6). Coulombic interactions between the anionic framework and the interlayer NMe_4^+ cations are stronger than the interlayer van der Waals interactions found in layered materials that have been successfully exfoliated down to monolayers.[3] Given that **1** can be electrochemically oxidized to the charge-neutral framework

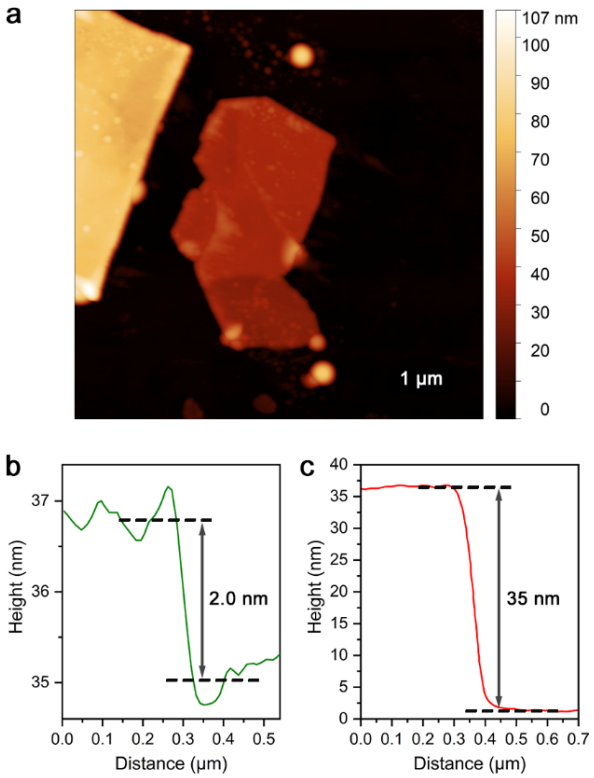

Figure 6. (a) Tapping mode atomic force microscopy (AFM) image of a mechanically exfoliated flake of **2** on SiO_2. **(b,c)** Cross-sectional AFM profiles showing (b) the height of a bilayer step in the middle of the crystal (path indicated by the green line on the top image) or (c) the overall thickness of the exfoliated flake (path indicated by the red line on the top image).

Fe_2L_3,[55] it will likely be possible to oxidize **2** through chemical or electrochemical methods to enable exfoliation to the monolayer limit. While the neutral framework is likely to possess much weaker magnetic interactions, electrical gating of monolayers of **2** could be used to tune the level of doping and the magnetic ordering temperature.[81]

CONCLUSIONS

The foregoing results demonstrate the presence of strong uniaxial magnetic anisotropy in the layered, semiconducting metal–organic framework material $(NMe_4)_2Fe_2L_3$. Despite the presence of isotropic $S = {}^5/_2$ Fe^{III} ions and organic radicals, this material displays much greater magnetic hysteresis than is observed in materials with similar crystal and electronic structures. The magnetic anisotropy energy calculated from oriented-crystal magnetization measurements is comparable to those of other layered materials that maintain their ferromagnetism to the 2D limit. DFT calculations indicate that the magnetic anisotropy of **2** arises from metal–ligand covalency and partial ligand-to-metal charge transfer. Together, these findings suggest **2** as a candidate for 2D magnetic order and highlight its potential use as a 2D magnetic semiconductor with gate-tunable magnetism and charge transport.

Ongoing work is focused on further exfoliating crystals of **2** and related materials for magneto-optical and transport measurements of both single crystals and thin flakes. Furthermore, it may be possible to increase the magnetic anisotropy and magnetic ordering temperature of these

frameworks through metal or ligand substitution. In particular, the installation of amide-based linkers through a recently reported post-synthetic procedure could greatly enhance the metal–ligand covalency, increasing both the metal–radical coupling and the extent of ligand-to-metal charge transfer.[50] This approach may also be applicable to the design of metal–organic single-chain magnets, as exemplified by a related 1D iron–chloranilate chain displaying slow magnetic relaxation.[82]

Broadly, these results illustrate an emerging general route for synthesizing 2D magnets, which targets layered metal–organic frameworks with energy-matched metal- and linker-based molecular orbitals. The growth of single crystals of other recently reported layered metal–organic magnets will enable additional insights into the importance of metal–ligand covalency on magnetic anisotropy in these materials,[34,37] and computational screening may identify new synthetic targets that could display magnetic order at much higher temperatures.

ASSOCIATED CONTENT

Supporting Information

The Supporting Information is available free of charge on the ACS Publications website.

Additional experimental details and characterization data (PDF)
Crystallographic data for **2** (CIF)

AUTHOR INFORMATION

Corresponding Authors

*dharris@berkeley.edu
*danilo.puggioni@northwestern.edu
*jrondinelli@northwestern.edu
*danna.freedman@northwestern.edu
*jrlong@berkeley.edu

ORCID

Yiran Wang: 0000-0002-3642-2294
Michael E. Ziebel: 0000-0003-1857-8292
Lei Sun: 0000-0001-8467-6750
J. Tyler Gish: 0000-0001-8429-5800
Tyler J. Pearson: 0000-0002-9883-506X
Agnes E. Thorarinsdottir: 0000-0001-9378-4454
Mark C. Hersam: 0000-0003-5120-1426
Jeffrey R. Long: 0000-0002-5234-1321
Danna E. Freedman: 0000-0002-2579-8835
James M. Rondinelli: 0000-0003-0508-2175
Danilo Puggioni: 0000-0002-2128-4191
T. David Harris: 0000-0003-4144-900X

Author Contributions

§Y.W. and M.E.Z. contributed equally to this work.

Notes

The authors declare no competing financial interest.

ACKNOWLEDGEMENT

This research was supported by the Department of Energy under Award DE-SC0019356. L.S. thanks the Postdoctoral Program in Environmental Chemistry Award from the Camille and Henry Dreyfus Foundation. Purchase of the SQUID magnetometer was supported in part by the International Institute of Nanotechnology (IIN). The X-ray crystallography made use of the Integrated Molecular Structure Education and Research Center (IMSERC) at Northwestern University, which is supported by the Soft and Hybrid Nanotechnology Experimental (SHyNE) Resource (NSF NNCI-1542205), the State of Illinois, and IIN. This work made use of the Electron Probe Instrumentation Center (EPIC) facility and the Keck Biophysics Facility of Northwestern University Atomic and Nanoscale Characterization Experimental (NUANCE) Center which is supported by SHyNE Resource (NSF ECCS-1542205), the Materials Research Science and Engineering Center (DMR-1720139), the State of Illinois, and Northwestern University. Quantitative analysis of Fe was performed at the Northwestern University Quantitative Bioelement Imaging Center (QBIC). This work used resources at the National Energy Research Scientific Computing Center, a DOE Office of Science User Facility supported by the Office of Science of the U.S. Department of Energy under Contract No. DE-AC02-05CH11231. We thank Prof. T. V. O'Halloran, Dr. J. A. DeGayner, and Dr. A. B. Altman for helpful discussions, and Dr. C. D. Malliakas, Dr. J. P. S. Walsh, and Dr. L. Liu for experimental assistance.

REFERENCES

(1) Novoselov, K. S. Electric Field Effect in Atomically Thin Carbon Films. *Science* **2004**, *306*, 666–669.
(2) Novoselov, K. S.; Jiang, D.; Schedin, F.; Booth, T. J.; Khotkevich, V. V.; Morozov, S. V.; Geim, A. K. Two-Dimensional Atomic Crystals. *Proc. Natl. Acad. Sci. U. S. A.* **2005**, *102*, 10451–10453.
(3) Ajayan, P.; Kim, P.; Banerjee, K. Two-Dimensional van Der Waals Materials. *Phys. Today* **2016**, *69*, 38–44.
(4) Novoselov, K. S.; Geim, A. K.; Morozov, S. V.; Jiang, D.; Katsnelson, M. I.; Grigorieva, I. V.; Dubonos, S. V.; Firsov, A. A. Two-Dimensional Gas of Massless Dirac Fermions in Graphene. *Nature* **2005**, *438*, 197–200.
(5) Mak, K. F.; Lee, C.; Hone, J.; Shan, J.; Heinz, T. F. Atomically Thin MoS_2: A New Direct-Gap Semiconductor. *Phys. Rev. Lett.* **2010**, *105*, 2–5.
(6) Bediako, D. K.; Rezaee, M.; Yoo, H.; Larson, D. T.; Zhao, S. Y. F.; Taniguchi, T.; Watanabe, K.; Brower-Thomas, T. L.; Kaxiras, E.; Kim, P. Heterointerface Effects in the Electro-Intercalation of van Der Waals Heterostructures. *Nature* **2018**, *558*, 425–429.
(7) Geim, A. K.; Grigorieva, I. V. Van Der Waals Heterostructures. *Nature* **2013**, *499*, 419–425.
(8) Novoselov, K. S.; Mishchenko, A.; Carvalho, A.; Castro Neto, A. H. 2D Materials and van Der Waals Heterostructures. *Science* **2016**, *353*.
(9) Balents, L.; Dean, C. R.; Efetov, D. K.; Young, A. F. Superconductivity and Strong Correlations in Moiré Flat Bands. *Nat. Phys*. **2020**, *16*, 725–733.
(10) Huang, B.; McGuire, M. A.; May, A. F.; Xiao, D.; Jarillo-Herrero, P.; Xu, X. Emergent Phenomena and Proximity Effects in 2D Magnets and Heterostructures. *Nat. Mater*. **2020**, *19*, 1276–1289.
(11) Huang, B.; Clark, G.; Navarro-Moratalla, E.; Klein, D. R.; Cheng, R.; Seyler, K. L.; Zhong, D.; Schmidgall, E.; McGuire, M. A.; Cobden, D. H.; Yao, W.; Xiao, D.; Jarillo-Herrero, P.; Xu, X. Layer-Dependent Ferromagnetism in a van Der Waals Crystal down to the Monolayer Limit. *Nature* **2017**, *546*, 270–273.
(12) Gong, C.; Li, L.; Li, Z.; Ji, H.; Stern, A.; Xia, Y.; Cao, T.; Bao, W.; Wang, C.; Wang, Y.; Qiu, Z. Q.; Cava, R. J.; Louie, S. G.; Xia, J.; Zhang, X. Discovery of Intrinsic Ferromagnetism in Two-Dimensional van Der Waals Crystals. *Nature* **2017**, *546*, 265–269.
(13) Fei, Z.; Huang, B.; Malinowski, P.; Wang, W.; Song, T.; Sanchez, J.; Yao, W.; Xiao, D.; Zhu, X.; May, A. F.; Wu, W.; Cobden, D. H.; Chu, J.-H.; Xu, X. Two-Dimensional Itinerant Ferromagnetism in Atomically Thin Fe_3GeTe_2. *Nat. Mater*. **2018**, *17*, 778–782.
(14) Huang, B.; Clark, G.; Klein, D. R.; MacNeill, D.; Navarro-Moratalla, E.; Seyler, K. L.; Wilson, N.; McGuire, M. A.; Cobden,

D. H.; Xiao, D.; Yao, W.; Jarillo-Herrero, P.; Xu, X. Electrical Control of 2D Magnetism in Bilayer CrI_3. *Nat. Nanotechnol.* **2018**, *13*, 544–548.
(15) Jiang, S.; Shan, J.; Mak, K. F. Electric-Field Switching of Two-Dimensional van Der Waals Magnets. *Nat. Mater.* **2018**, *17*, 406–410.
(16) Song, T.; Cai, X.; Tu, M. W.; Zhang, X.; Huang, B.; Wilson, N. P.; Seyler, K. L.; Zhu, L.; Taniguchi, T.; Watanabe, K.; McGuire, M. A.; Cobden, D. H.; Xiao, D.; Yao, W.; Xu, X. Giant Tunneling Magnetoresistance in Spin-Filter van Der Waals Heterostructures. *Science* **2018**, *360*, 1214–1218.
(17) Zhang, X.; Li, L.; Weber, D.; Goldberger, J.; Mak, K. F. Gate-Tunable Spin Waves in Antiferromagnetic Atomic Bilayers. *Nat. Mater.* **2020**, *19*, 838–842.
(18) Ohno, Y.; Young, D. K.; Beschoten, B.; Matsukura, F.; Ohno, H.; Awschalom, D. D. Electrical Spin Injection in a Ferromagnetic Semiconductor Heterostructure. *Nature* **1999**, *402*, 790–792.
(19) Yamanouchi, M.; Chiba, D.; Matsukura, F.; Ohno, H. Current-Induced Domain-Wall Switching in a Ferromagnetic Semiconductor Structure. *Nature* **2004**, *428*, 539–541.
(20) Awschalom, D. D.; Flatté, M. E. Challenges for Semiconductor Spintronics. *Nat. Phys*. **2007**, *3*, 153–159.
(21) Ohno, H.; Chiba, D.; Matsukura, F.; Omiya, T.; Abe, E.; Dietl, T.; Ohno, Y.; Ohtani, K. Electric-Field Control of Ferromagnetism. *Nature* **2000**, *408*, 944–946.
(22) Chiba, D.; Yamanouchi, H.; Hatsukura, F.; Ohno, H. Electrical Manipulation of Magnetization Reversal in a Ferromagnetic Semiconductor. *Science* **2003**, *301*, 943–945.
(23) Gibertini, M.; Koperski, M.; Morpurgo, A. F.; Novoselov, K. S. Magnetic 2D Materials and Heterostructures. *Nat. Nanotechnol*. **2019**, *14*, 408–419.
(24) Li, H.; Ruan, S.; Zeng, Y. J. Intrinsic Van Der Waals Magnetic Materials from Bulk to the 2D Limit: New Frontiers of Spintronics. *Adv. Mater*. **2019**, *31*, 1900065.
(25) Telford, E. J.; Dismukes, A. H.; Lee, K.; Cheng, M.; Wieteska, A.; Bartholomew, A. K.; Chen, Y. S.; Xu, X.; Pasupathy, A. N.; Zhu, X.; Dean, C. R.; Roy, X. Layered Antiferromagnetism Induces Large Negative Magnetoresistance in the van Der Waals Semiconductor CrSBr. *Adv. Mater*. **2020**, *32*, 2003240.
(26) Zhou, H. C.; Long, J. R.; Yaghi, O. M. Introduction to Metal-Organic Frameworks. *Chem. Rev*. **2012**, *112*, 673–674.
(27) Xie, L. S.; Skorupskii, G.; Dincă, M. Electrically Conductive Metal–Organic Frameworks. *Chem. Rev*. **2020**, *120*, 8536–8580.
(28) Mínguez Espallargas, G.; Coronado, E. Magnetic Functionalities in MOFs: From the Framework to the Pore. *Chem. Soc. Rev*. **2018**, *47*, 533–557.
(29) Hendon, C. H.; Tiana, D.; Fontecave, M.; Sanchez, C.; D'Arras, L.; Sassoye, C.; Rozes, L.; Mellot-Draznieks, C.; Walsh, A. Engineering the Optical Response of the Titanium-MIL-125 Metal-Organic Framework through Ligand Functionalization. *J. Am. Chem. Soc*. **2013**, *135*, 10942–10945.
(30) Motokawa, N.; Matsunaga, S.; Takaishi, S.; Miyasaka, H.; Yamashita, M.; Dunbar, K. R. Reversible Magnetism between an Antiferromagnet and a Ferromagnet Related to Solvation/Desolvation in a Robust Layered $[Ru_2]_2TCNQ$ Charge-Transfer System. *J. Am. Chem. Soc*. **2010**, *132*, 11943–11951.
(31) Zhao, M.; Wang, A.; Zhang, X. Half-Metallicity of a Kagome Spin Lattice: The Case of a Manganese Bis-Dithiolene Monolayer. *Nanoscale* **2013**, *5*, 10404.
(32) DeGayner, J. A.; Jeon, I.; Sun, L.; Dincă, M.; Harris, T. D. 2D Conductive Iron-Quinoid Magnets Ordering up to T_c = 105 K via Heterogenous Redox Chemistry. *J. Am. Chem. Soc*. **2017**, *139*, 4175–4184.
(33) López-Cabrelles, J.; Mañas-Valero, S.; Vitórica-Yrezábal, I. J.; Bereciartua, P. J.; Rodríguez-Velamazán, J. A.; Waerenborgh, J. C.; Vieira, B. J. C.; Davidovikj, D.; Steeneken, P. G.; van der Zant, H. S. J.; Mínguez Espallargas, G.; Coronado, E. Isoreticular Two-Dimensional Magnetic Coordination Polymers Prepared through Pre-Synthetic Ligand Functionalization. *Nat. Chem*. **2018**, *10*, 1001–1007.
(34) Pedersen, K. S.; Perlepe, P.; Aubrey, M. L.; Woodruff, D. N.; Reyes-Lillo, S. E.; Reinholdt, A.; Voigt, L.; Li, Z.; Borup, K.; Rouzières, M.; Samohvalov, D.; Wilhelm, F.; Rogalev, A.; Neaton, J. B.; Long, J. R.; Clérac, R. Formation of the Layered Conductive Magnet $CrCl_2(Pyrazine)_2$ through Redox-Active Coordination Chemistry. *Nat. Chem*. **2018**, *10*, 1056–1061.
(35) Yang, C.; Dong, R.; Wang, M.; Petkov, P. St.; Zhang, Z.; Wang, M.; Han, P.; Ballabio, M.; Bräuninger, S. A.; Liao, Z.; Zhang, J.; Schwotzer, F.; Zschech, E.; Klauss, H.-H.; Cánovas, E.; Kaskel, S.; Bonn, M.; Zhou, S.; Heine, T.; Feng, X. A Semiconducting Layered Metal-Organic Framework Magnet. *Nat. Commun*. **2019**, *10*, 3260.
(36) Thorarinsdottir, A. E.; Harris, T. D. Metal–Organic Framework Magnets. *Chem. Rev*. **2020**, *120*, 8716–8789.
(37) Perlepe, P.; Oyarzabal, I.; Mailman, A.; Yquel, M.; Platunov, M.; Dovgaliuk, I.; Rouzières, M.; Négrier, P.; Mondieig, D.; Suturina, E. A.; Dourges, M.-A.; Bonhommeau, S.; Musgrave, R. A.; Pedersen, K. S.; Chernyshov, D.; Wilhelm, F.; Rogalev, A.; Mathonière, C.; Clérac, R. Metal-Organic Magnets with Large Coercivity and Ordering Temperatures up to 242°C. *Science* **2020**, *370*, 587–592.
(38) Mermin, N. D.; Wagner, H. Absence of Ferromagnetism or Antiferromagnetism in One- or Two-Dimensional Isotropic Heisenberg Models. *Phys. Rev. Lett*. **1966**, *17*, 1133–1136.
(39) Heinrich, B.; Urquhart, K. B.; Arrott, A. S.; Cochran, J. F.; Myrtle, K.; Purcell, S. T. Ferromagnetic-Resonance Study of Ultrathin Bcc Fe(100) Films Grown Epitaxially on Fcc Ag(100) Substrates. *Phys. Rev. Lett*. **1987**, *59*, 1756–1759.
(40) Lado, J. L.; Fernández-Rossier, J. On the Origin of Magnetic Anisotropy in Two Dimensional CrI_3. *2D Mater*. **2017**, *4*, 035002.
(41) Richter, N.; Weber, D.; Martin, F.; Singh, N.; Schwingenschlögl, U.; Lotsch, B. V.; Kläui, M. Temperature-Dependent Magnetic Anisotropy in the Layered Magnetic Semiconductors CrI_3 and $CrBr_3$. *Phys. Rev. Mater*. **2018**, *2*, 024004.
(42) Seo, J.; Kim, D. Y.; An, E. S.; Kim, K.; Kim, G.-Y.; Hwang, S.-Y.; Kim, D. W.; Jang, B. G.; Kim, H.; Eom, G.; Seo, S. Y.; Stania, R.; Muntwiler, M.; Lee, J.; Watanabe, K.; Taniguchi, T.; Jo, Y.-J.; Lee, J.; Min, B. I.; Jo, M. H.; Yeom, H. W.; Choi, S.-Y.; Shim, J. H.; Kim, J. S. Nearly Room Temperature Ferromagnetism in a Magnetic Metal-Rich van der Waals Metal. *Sci. Adv*. **2020**, *6*, eaay8912.
(43) Skomski, R.; Sellmyer, D. J. Anisotropy of Rare-Earth Magnets. *J. Rare Earths* **2009**, *27*, 675–679.
(44) Yang, B.; Zhang, X.; Yang, H.; Han, X.; Yan, Y. Nonmetallic Atoms Induced Magnetic Anisotropy in Monolayer Chromium Trihalides. *J. Phys. Chem. C* **2019**, *123*, 691–697.
(45) Kitagawa, S. Coordination Compounds of 1,4-Dihydroxybenzoquinone and Its Homologues. Structures and Properties. *Coord. Chem. Rev*. **2002**, *224*, 11–34.
(46) Shilov, G. V.; Nikitina, Z. K.; Ovanesyan, N. S.; Aldoshin, S. M.; Makhaev, V. D. Phenazineoxonium Chloranilatomanganate and Chloranilatoferrate: Synthesis, Structure, Magnetic Properties, and Mössbauer *Spectra. Russ. Chem. Bull*. **2011**, *60*, 1209–1219.
(47) Atzori, M.; Benmansour, S.; Mínguez Espallargas, G.; Clemente-León, M.; Abhervé, A.; Gómez-Claramunt, P.; Coronado, E.; Artizzu, F.; Sessini, E.; Deplano, P.; Serpe, A.; Mercuri, M. L.; Gómez García, C. J. A Family of Layered Chiral Porous Magnets Exhibiting Tunable Ordering Temperatures. *Inorg. Chem*. **2013**, *52*, 10031–10040.
(48) Jeon, I. R.; Negru, B.; Van Duyne, R. P.; Harris, T. D. A 2D Semiquinone Radical-Containing Microporous Magnet with Solvent-Induced Switching from T_c = 26 to 80 K. *J. Am. Chem. Soc*. **2015**, *137*, 15699–15702.
(49) Ziebel, M. E.; Darago, L. E.; Long, J. R. Control of Electronic Structure and Conductivity in Two-Dimensional Metal–Semiquinoid Frameworks of Titanium, Vanadium, and Chromium. *J. Am. Chem. Soc*. **2018**, *140*, 3040–3051.
(50) Liu, L.; Li, L.; Ziebel, M. E.; Harris, T. D. Metal-Diamidobenzoquinone Frameworks via Post-Synthetic Linker Exchange. *J. Am. Chem. Soc*. **2020**, *142*, 4705–4713.
(51) Collins, K. A.; Saballos, R. J.; Fataftah, M. S.; Puggioni, D.; Rondinelli, J. M.; Freedman, D. E. Synthetic Investigation of Competing Magnetic Interactions in 2D Metal–Chloranilate Radical Frameworks. *Chem. Sci*. **2020**, 5922–5928.

(52) van Koeverden, M. P.; Abrahams, B. F.; D'Alessandro, D. M.; Doheny, P. W.; Hua, C.; Hudson, T. A.; Jameson, G. N. L.; Murray, K. S.; Phonsri, W.; Robson, R.; Sutton, A. L. Tuning Charge-State Localization in a Semiconductive Iron(III)–Chloranilate Framework Magnet Using a Redox-Active Cation. *Chem. Mater*. **2020**, *32*, 7551–7563.
(53) Taniguchi, K.; Chen, J.; Sekine, Y.; Miyasaka, H. Magnetic Phase Switching in a Tetraoxolene-Bridged Honeycomb Ferrimagnet Using a Lithium Ion Battery System. *Chem. Mater*. **2017**, *29*, 10053–10059.
(54) Liu, L.; DeGayner, J. A.; Sun, L.; Zee, D. Z.; Harris, D. Reversible Redox Switching of Magnetic Order and Electrical Conductivity in a 2D Manganese Benzoquinoid Framework. *Chem. Sci*. **2019**, *10*, 4652–4661.
(55) Ziebel, M. E.; Gaggioli, C. A.; Turkiewicz, A. B.; Ryu, W.; Gagliardi, L.; Long, J. R. Effects of Covalency on Anionic Redox Chemistry in Semiquinoid-Based Metal-Organic Frameworks. *J. Am. Chem. Soc*. **2020**, *142*, 2653–2664.
(56) Cullity, B. D.; Graham, C. D. *Introduction to Magnetic Materials*; John Wiley & Sons, Inc.: Hoboken, NJ, USA, 2008; pp. 197–239.
(57) Darago, L. E.; Aubrey, M. L.; Yu, C. J.; Gonzalez, M. I.; Long, J. R. Electronic Conductivity, Ferrimagnetic Ordering, and Reductive Insertion Mediated by Organic Mixed-Valence in a Ferric Semiquinoid Metal–Organic Framework. *J. Am. Chem. Soc*. **2015**, *137*, 15703–15711.
(58) Stoner, E. C.; Wohlfarth, E. P. A Mechanism of Magnetic Hysteresis in Heterogeneous Alloys. *Philos. Trans. R. Soc. A* **1948**, *240*, 599–642.
(59) Sharma, S.; Radulov, I.; Major, M.; Alff, L. Evolution of Magnetic Anisotropy with Sm Contents in Sm-Co Thin Films. *IEEE Trans. Magn*. **2018**, *54*, 1-5.
(60) Manriquez, J. M.; Yee, G. T.; McLean, R. S.; Epstein, A. J.; Miller, J. S. A Room-Temperature Molecular/Organic-Based Magnet. *Science* **1991**, *252*, 1415–1417.
(61) Zhang, J.; Ensling, J.; Ksenofontov, V.; Gütlich, P.; Epstein, A. J.; Miller, J. S. Molecule-Based Magnets with T_c Values Above 100 K and Coercive Fields up to 6500 Oe. *Angew. Chem. Int. Ed*. **1998**, *37*, 657–660.
(62) Coronado, E.; Galán-Mascarós, J. R.; Gómez-García, C. J.; Martínez-Agudo, J. M. Increasing the Coercivity in Layered Molecular-Based Magnets $A[M^{II}M^{III}(Ox)_3]$ (M^{II} = Mn, Fe, Co, Ni, Cu; M^{III} = Cr, Fe; Ox = Oxalate; A = Organic or Organometallic Cation). *Adv. Mater*. **1999**, *11*, 558–561.
(63) Rittenberg, D. K.; Sugiura, K.; Sakata, Y.; Mikami, S.; Epstein, A. J.; Miller, J. S. Large Coercivity and High Remanent Magnetization Organic-Based Magnets. *Adv. Mater*. **2000**, *12*, 126–130.
(64) Motokawa, N.; Oyama, T.; Matsunaga, S.; Miyasaka, H.; Yamashita, M.; Dunbar, K. R. Charge-Transfer Two-Dimensional Layers Constructed from a 2:1 Assembly of Paddlewheel Diruthenium (II,II) Complexes and Bis[1,2,5]-Thiadizolotetracyanoquinodimethane: Bulk Magnetic Behavior as a Function of Inter-Layer Interactions. *CrystEngComm* **2009**, *11*, 2121.
(65) Chen, J.; Taniguchi, K.; Sekine, Y.; Miyasaka, H. *J. Magn. Magn. Mater*. **2020**, *494*, 165818.
(66) Sucksmith, W.; Thompson, J. E. The Magnetic Anisotropy of Cobalt. *Proc. R. Soc. London. Ser. A* **1954**, *225*, 362–375.
(67) Bolyachkin, A. S.; Neznakhin, D. S.; Bartashevich, M. I. The Effect of Magnetization Anisotropy and Paramagnetic Susceptibility on the Magnetization Process. *J. Appl. Phys*. **2015**, *118*, 213902.
(68) Zener, C. Classical Theory of the Temperature Dependence of Magnetic Anisotropy Energy. *Phys. Rev*. **1954**, *96*, 1335–1337.
(69) Carr, W. J. Temperature Dependence of Ferromagnetic Anisotropy. *J. Appl. Phys*. **1958**, *29*, 436–437.
(70) Xing, W.; Chen, Y.; Odenthal, P. M. Magnetic Anisotropy of the Single-Crystalline Ferromagnetic Insulator $Cr_2Ge_2Te_6$. *Japanese J. Appl. Phys*. **2016**, *55*, 33001.
(71) Zhang, J. T.; Lu, X. M.; Zhou, J.; Sun, H.; Su, J.; Ju, C. C.; Huang, F. Z.; Zhu, J. S. Origin of Magnetic Anisotropy and Spiral Spin Order in Multiferroic $BiFeO_3$. *Appl. Phys. Lett*. **2012**, *100*, 242413.
(72) Pearson, R. F. Magnetocrystalline Anisotropy of Rare-Earth Iron Garnets. In Proceedings of the Seventh Conference on Magnetism and Magnetic Materials; Springer US: Boston, MA, **1962**; pp 1236–1242.
(73) Ohhashi, K.; Tsujikawa, I. Magnetic Properties of $FeCl_3$-Graphite Compounds. II. Magnetic Susceptibilities. *J. Phys. Soc. Japan* **1974**, *36*, 980–988.
(74) Pullar, R. C. Hexagonal Ferrites: A Review of the Synthesis, Properties and Applications of Hexaferrite Ceramics. *Prog. Mater. Sci*. **2012**, *57*, 1191–1334.
(75) Casimir, H. B. G.; Smit, J.; Enz, U.; Fast, J. F.; Wijn, H. P. J.; Gorter, E. W.; Duyvesteyn, A. J. W.; Fast, J. D.; de Jong, J. J. Report of Some Research in the Field of Magnetism at the Philips Laboratories. *J. Phys. Radium* **1959**, *20*, 360–373.
(76) Fuchikami, N. Magnetic Anisotropy of Magnetoplumbite $BaFe_{12}O_{19}$. J. *Phys. Soc. Japan* **1965**, *20*, 760–769.
(77) Marzari, N.; Mostofi, A. A.; Yates, J. R.; Souza, I.; Vanderbilt, D. Maximally Localized Wannier Functions: Theory and Applications. *Rev. Mod. Phys*. **2012**, *84*, 1419–1475.
(78) Mostofi, A. A.; Yates, J. R.; Pizzi, G.; Lee, Y.-S.; Souza, I.; Vanderbilt, D.; Marzari, N. An Updated Version of Wannier90: A Tool for Obtaining Maximally-Localised Wannier Functions. *Comput. Phys. Commun*. **2014**, *185*, 2309–2310.
(79) Benmansour, S.; Abhervé, A.; Gómez-Claramunt, P.; Vallés-García, C.; Gómez-García, C. J. Nanosheets of Two-Dimensional Magnetic and Conducting Fe(II)/Fe(III) Mixed-Valence Metal-Organic Frameworks. *ACS Appl. Mater. Interfaces* **2017**, *9*, 26210–26218.
(80) Ziebel, M. E.; Ondry, J. C.; Long, J. R. Two-Dimensional, Conductive Niobium and Molybdenum Metal–Organic Frameworks. *Chem. Sci*. **2020**, *11*, 6690–6700.
(81) Zhang, Y.; Chen, X. H.; Yu, Y.; Wang, N. Z.; Yi, Y.; Sun, Z.; Zhang, J.; Wu, Y. Z.; Zhu, J.; Wang, J.; Deng, Y.; Wu, S.; Song, Y. Gate-Tunable Room-Temperature Ferromagnetism in Two-Dimensional Fe_3GeTe_2. *Nature* **2018**, *563*, 94–99.
(82) DeGayner, J. A.; Wang, K.; Harris, T. D. A Ferric Semiquinoid Single-Chain Magnet via Thermally-Switchable Metal–Ligand Electron Transfer. *J. Am. Chem. Soc*. **2018**, *140*, 6550–6553.

For Table of Contents Only:

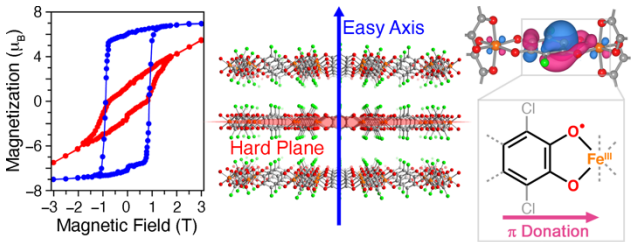

Metal–Ligand Covalency Generates Magnetic Anisotropy